AGU PUBLICATIONS

JGR

Journal of Geophysical Research: Atmospheres

RESEARCH ARTICLE
10.1002/2017JD027457

Key Points:
- The transition from shallow cumulus to congestus is governed by destabilization of the thermodynamic profiles
- The evolution of traditional stability measures by themselves is not able to explain differences in the simulations
- Conditionally sampled cloud properties (in particular, mean cloud buoyancy) are able to show the differences among the simulations

Correspondence to:
D. B. Mechem,
dmechem@ku.edu

Citation:
Mechem, D. B., & Giangrande, S. E. (2018). The challenge of identifying controls on cloud properties and precipitation onset for cumulus congestus sampled during MC3E. *Journal of Geophysical Research: Atmospheres*, *123*. https://doi.org/10.1002/2017JD027457

Received 14 JUL 2017
Accepted 23 FEB 2018
Accepted article online 1 MAR 2018

The Challenge of Identifying Controls on Cloud Properties and Precipitation Onset for Cumulus Congestus Sampled During MC3E

David B. Mechem[1] **and Scott E. Giangrande**[2]

[1]Department of Geography and Atmospheric Science, University of Kansas, Lawrence, KS, USA, [2]Environmental and Climate Sciences Department, Brookhaven National Laboratory, Upton, NY, USA

Abstract Controls on precipitation onset and the transition from shallow cumulus to congestus are explored using a suite of 16 large-eddy simulations based on the 25 May 2011 event from the Midlatitude Continental Convective Clouds Experiment (MC3E). The thermodynamic variables in the model are relaxed at various timescales to observationally constrained temperature and moisture profiles in order to better reproduce the observed behavior of precipitation onset and total precipitation. Three of the simulations stand out as best matching the precipitation observations and also perform well for independent comparisons of cloud fraction, precipitation area fraction, and evolution of cloud top occurrence. All three simulations exhibit a destabilization over time, which leads to a transition to deeper clouds, but the evolution of traditional stability metrics by themselves is not able to explain differences in the simulations. Conditionally sampled cloud properties (in particular, mean cloud buoyancy), however, do elicit differences among the simulations. The inability of environmental profiles alone to discern subtle differences among the simulations and the usefulness of conditionally sampled model quantities argue for hybrid observational/modeling approaches. These combined approaches enable a more complete physical understanding of cloud systems by combining observational sampling of time-varying three-dimensional meteorological quantities and cloud properties, along with detailed representation of cloud microphysical and dynamical processes from numerical models.

1. Introduction

Global Climate Models (GCMs) continue to struggle representing boundary layer clouds (stratocumulus and shallow cumulus) (Bony & Dufresne, 2005; Medeiros et al., 2008; Medeiros & Stevens, 2011; Song et al., 2013; Stevens & Bony, 2013; Wyant et al., 2007) and the transitions to deeper cloud types (Dai, 2006; Del Genio & Wu, 2010; Kim et al., 2010; Yuan et al., 2013). Stratocumulus clouds scatter much of the incoming solar radiation back to space and therefore exert a cooling effect on the climate system. In the trade latitudes, vertical transports from shallow cumulus balance the large-scale subsidence and set the equilibrium depth of the boundary layer. Over the continent, the deepening of shallow cumulus clouds is an intrinsic part of the diurnal cycle of convection, with shallow cumulus, under the right conditions, deepening into congestus and eventually to cumulonimbus. In the midlatitudes, shallow stratocumulus and cumulus systems are a robust signal of baroclinic waves (Field & Wood, 2007) and, from the framework of a fixed geographic location, are a highly transient component of synoptic wave passage.

Difficulty in representing cloud and cloud transitions also extends to high-resolution cloud process models that are used to construct data sets employed for formulating and evaluating GCM cloud dynamical and microphysical process parameterizations (e.g., Grabowski et al., 2006; Stevens et al., 2005; van Zanten et al., 2011). A number of these model intercomparison studies have been conducted over the years, focused mainly on highly idealized model configurations of weakly forced cloud systems (Ackerman et al., 2009; Brown et al., 2002; Siebesma et al., 2003; Stevens et al., 2001, 2005; van Zanten et al., 2011) where cloud evolution is not predominantly governed by synoptic-scale forcing. These large-eddy simulation (LES) models assume horizontally homogeneous initial conditions, and any external forcing is typically applied evenly across the model domain. In effect, this imposes a constraint of statistical homogeneity over the LES domain. Model intercomparisons of cumulus transitions are predominantly forced using the diurnal cycle in surface fluxes while also assuming large-scale homogeneity and hence weak horizontal advective tendencies (e.g., Brown et al., 2002; Grabowski et al., 2006).

The combination of Lagrangian frameworks and/or weak forcing found in the previous studies negates the importance of advective forcing terms. This is a desirable simplification but one that is typically only justified in quiescent or near-barotropic conditions. Moreover, this assumption is not appropriate for situations having strong shear associated with baroclinic synoptic systems, and it precludes exploration of transient cloud systems associated with substantial synoptic-scale or mesoscale variability. Examples of systems for which this idealized framework is not appropriate include deepening cumulus in the warm sector or postcold frontal stratocumulus and cumulus congestus (e.g., Kollias & Albrecht, 2000; Mechem et al., 2010, 2015).

In contrast, an Eulerian modeling framework is ideal for comparisons with fixed sites such as the Department of Energy (DOE) Atmospheric Radiation Measurement (ARM) program Southern Great Plains (SGP) site in northern Oklahoma (e.g., Mather & Voyles, 2013). An Eulerian modeling approach requires forcing terms in the form of horizontal advective tendencies of temperature and moisture, in addition to the large-scale vertical motion and surface fluxes required in the Lagrangian approach. These forcings can be supplied by the variational analysis method of Zhang and Lin (1997), which incorporates ARM observations together with numerical weather prediction (NWP) analysis to create observationally constrained forcing tendencies (Xie et al., 2014). This ARM variational analysis product has been used extensively in process-modeling studies (e.g., Khairoutdinov & Randall, 2003; Mechem et al., 2015; Xie et al., 2005; Xu et al., 2002, 2005). LES fields produced under this approach represent a semidiagnostic response to the large-scale forcing and follow an assumption of a separation of scales between the large-scale forcing fields and the cloud response. Temporally, this assumption corresponds to cloud microphysical and dynamical responses occurring on timescales shorter than the forcing. In cases of highly transient forcing (i.e., forcing timescale of the same order as the cloud response), this assumption can be violated and the framework may not be well posed.

Recently, Mechem et al. (2015) explored the impact of details in forcing for reproducing the temporal evolution of highly transient cloud system properties using high-resolution LES with size-resolving (bin) microphysics. In particular, they assessed the importance of using time-varying versus steady state forcing configurations and the impact of the spatial scale of the LES forcing. Advanced observational metrics, derived from newer ARM instrumentation including scanning cloud radar, indicate that time-varying forcing leads to model behavior better matched to the observed cloud field evolution. Those observations included cloud fraction, precipitation area fraction, precipitation onset time, probability distribution functions (PDFs) of cloud top height, and total precipitation. Although time-varying forcing configurations in Mechem et al. (2015) produced the best match with observations, including realistically deepening cloud systems and coexisting shallow cumulus and congestus, all the simulations exhibited flaws. Specifically, the transition from cumulus to congestus occurred more rapidly than the observed transition, and simulations overestimated areal-averaged precipitation rate and precipitation areal fraction. The better performing runs trended closer to the observed precipitation onset behavior, but even the best simulations produced precipitation too quickly, suggesting an overestimation of the large-scale forcing imposed by the NWP model at the heart of the variational analysis procedure.

The focus for this study is the further evaluation of the controls on the transition from shallow cumulus to congestus, the onset of precipitation, and subsequent evolution for the 25 May 2011 event. Mechem et al. (2015) indicated that this transition to congestus for the 25 May event appeared tied to the evolution of stability (combination of moisture and temperature) as a control on transition time (e.g., Xie et al., 2014; Zhang & Klein, 2013), which was improved through the use of time-varying forcing. In order to further constrain precipitation onset and total accumulation amounts, in this study we relax ("nudge") the simulations performed to the variationally constrained profiles of temperature and moisture used to formulate the initial conditions. This relaxation is one approach to compensate for excessive or poorly aligned forcing terms, in effect modifying the forcing details by steering the model toward the ARM observations incorporated into the variational analysis. As with the previous study, we similarly perform a suite of sensitivity simulations and focus on those that reproduce the best observed precipitation characteristics (onset time and accumulated precipitation). We then evaluate the morphology of those simulations against independent observations of cloud, precipitation, and other properties including fractional cloud and precipitation areal coverage, cloud profile behaviors, and thermodynamic evolution.

Previous studies of the controls for shallow-to-deep transition focused on the role of entrainment rate and cloud base mass flux (Grabowski et al., 2006) or the role of mean updraft buoyancy (Wu et al., 2009). We concentrate on the role of the evolving environmental stability as a control on the shallow-to-congestus

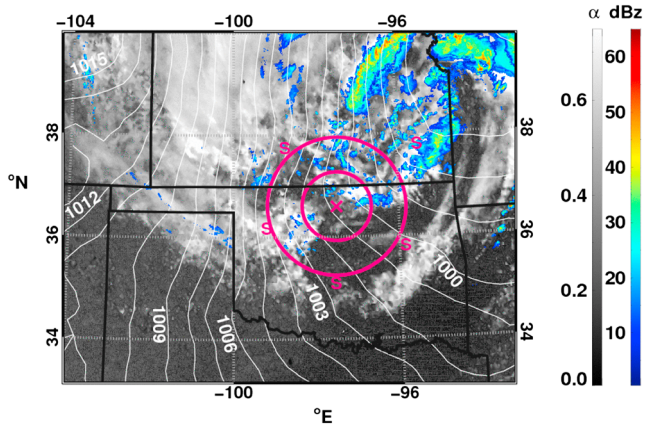

Figure 1. Synoptic configuration at 1800 UTC. Albedo from GOES visible satellite imagery is combined with isobars of the surface pressure field (in hPa) from North American Regional Reanalysis (Mesinger et al., 2006) and a multiradar composite of reflectivity from WSR-88D Next Generation Weather Radar (NEXRAD). The magenta cross represents the location of the ARM Central Facility, and the multiple S's indicate MC3E sounding sites. Concentric circles represent 75 and 150 km regions for the variational analysis and radar precipitation estimates. Adapted from Mechem et al. (2015).

transition, in particular attempting to identify features in the thermodynamic profiles that suggest imminent transition to deeper clouds, an exercise we find to be exceptionally difficult. We also explore the transition from the Wu et al. (2009) perspective of mean cloud buoyancy and find their approach to work well in identifying cloud transitions, moreso than looking at subtle changes in stability alone.

2. The 25 May 2011 Congestus Event

2.1. Synoptic Overview

The 25 May 2011 event was a strongly forced case of shallow cumulus transitioning to precipitating cumulus congestus. This case was observed during the DOE ARM and National Aeronautics and Space Administration (NASA) Global Precipitation Measurement mission campaign, the Midlatitude Continental Convective Clouds Experiment (MC3E) (Jensen et al., 2016). As summarized by Mechem et al. (2015), clouds developed following a frontal passage connected with a mature low-pressure system over central Kansas (Figure 1). Shallow clouds formed over the ARM Southern Great Plains (SGP) site by 1500 UTC (0900 CST). These clouds gradually transitioned to scattered cumulus congestus by midday (1800 UTC; 1200 CST) and commingled nonprecipitating clouds and precipitating congestus thereafter (see snapshots of the cloud field in Figure 2). Winds at cloud level naturally shifted from southwest to northwest as the low-pressure system progressed eastward by the afternoon (late UTC) hours.

During MC3E, radiosondes were launched at 3 h intervals from six locations a distance of approximately 150 km from the SGP Lamont, Oklahoma Central Facility (CF) (e.g., Jensen et al., 2015) (locations highlighted in Figure 1). Using the variational analysis method of Zhang and Lin (1997), these radiosondes contribute to an idealized perspective on the evolution of the MC3E synoptic conditions for that event (Xie et al., 2014). Variational analysis fields following those methods (centered on the SGP CF) serve as the forcing data set for the simulations presented in this study. Our control simulation employs a 75 km domain, time-varying forcing configuration as previously considered in Mechem et al. (2015), associated in that study with LES outputs having a more accurate depiction for event evolution across several cloud and precipitation observational data set metrics.

The gradual deepening of the cloud field from shallow cumulus to congestus may be attributed to several factors when considering those underlying forcing depictions, as presented in Figure 2 in Mechem et al. (2015). First, the northern Oklahoma region experienced positive low-level moisture advection (their Figure 2c; approximately surface to 640 hPa mean value of 0.15 g kg^{-1} h^{-1}) throughout the event. This moist advection included the moisture advected from the Gulf of Mexico wrapping around the mature low-pressure system. Throughout the day, a deep layer of cold advection (their Figure 2a, approximately surface to 640 hPa mean value of -0.35 K h^{-1}) brought the layer closer to saturation and likely also promoted cloud development. Finally, upward vertical motion overlaid low-level subsidence (their Figure 2e; approximately surface to 640 hPa mean value of -1.32 mb h^{-1}).

2.2. ARM SGP Observational Data Sets

Following Mechem et al. (2015), the 25 May 2011 event observational evaluations draw heavily from routine surface instrumentation and radar observations at the ARM SGP CF. The primary focus remains on evaluating LES macroscale cloud properties that follow naturally from LES model outputs without the need for advanced forward instrument simulators. For this study, those properties will include cloud fraction, precipitation onset timing, fractional cloud/precipitation coverages (including cloud top distributions), and total precipitation accumulations.

Cloud field visualizations for this study are generated from standard ARM ARSCL products (Active Remote Sensing of CLouds) (Atmospheric Radiation Measurement (ARM) Climate Research Facility, 2011a; Clothiaux et al., 2000; Kollias et al., 2005) that merge observations from the vertically pointing 35 GHz Ka-

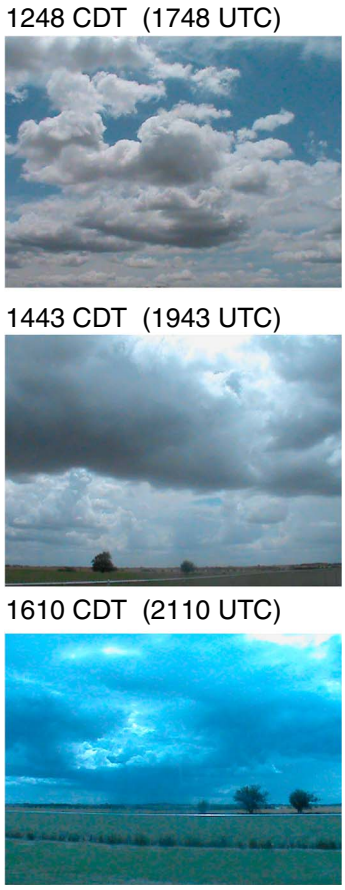

Figure 2. Snapshots of clouds in the vicinity of the ARM SGP CF on 25 May 2011.

band *Z*enith Radar (KAZR), collocated laser ceilometer, micropulse lidar, and microwave radiometer to identify cloud boundaries in the vertical profiles. ARM also deployed a first generation of dual-frequency 35/94 GHz (Ka/W-band) Scanning ARM Cloud Radars (SACRs) during MC3E (e.g., Atmospheric Radiation Measurement (ARM) Climate Research Facility, 2011b; Kollias et al., 2014). For that campaign, SACRs sampled cloud elements using 2-D slices (range-height; RHI) that could quickly track cloud features and evaluate their geometric properties in time (e.g., Borque et al., 2014). Additional details on the cloud observational data sets used for model evaluation in this study are found in Mechem et al. (2015).

Precipitating cell properties and onset behaviors to within 150 km of the SGP Lamont site are captured using the surveillance 5.4 GHz ARM C-band Scanning ARM Polarimetric weather Radar (C-SAPR) (e.g., Atmospheric Radiation Measurement (ARM) Climate Research Facility, 2011c; Giangrande et al., 2014) and surrounding NWS WSR-88D rainfall products. Precipitation area fraction was tracked from the C-SAPR data set by calculating the area covered by near-surface radar reflectivity factor *Z* exceeding minimum thresholds discussed below. To illustrate possible natural variability in these measurements, area fractions were estimated over a larger 150 km domain and a smaller 75 km domain centered on the ARM SGP CF. To allow for a range of radar measurement uncertainty under light rain conditions, this study also considers the spread of area fraction corresponding to a less restrictive 25 dB*Z* threshold and a more restrictive 30 dB*Z* threshold. The 30 dB*Z* value is based on previous studies of warm-season precipitation in the vicinity of the ARM SGP site, and the 5 dB offset roughly corresponds to typical radar calibration uncertainties (Giangrande et al., 2012, 2014). We also note the well-known nature of radar beam geometry where radar-based quantities like surface precipitation will be better represented closer to the radar. For domain-mean precipitation accumulation, we consider a standard gauge-adjusted WSR-88D radar rainfall product from the National Mosaic and Multi-Sensor Quantitative Precipitation Estimation (NMQ) archives (e.g., Zhang et al., 2005). These estimates are also calculated for the 150 km and 75 km domains centered on the ARM SGP CF.

3. LES Model and Simulation Configuration

The System for Atmospheric Modeling (SAM) (Khairoutdinov & Randall, 2003) is used for all simulations. The simulations share the same basic configuration from Mechem et al. (2015) as a starting point and employ a domain size of $38.3 \times 38.3 \times 8$ km^3 ($384 \times 384 \times 160$ points) with a horizontal grid spacing of 100 m and a uniform vertical grid spacing of 50 m. The lateral boundary conditions are doubly periodic. This grid configuration is a compromise between resolution and sufficient domain coverage to permit the emergence of mesoscale variability. Matheou et al. (2011) demonstrated a strong resolution dependence for simulations of Rain in Cumulus over the Ocean (RICO) (Rauber et al., 2007) trade cumulus and that precipitating LES solutions are not converged even for horizontal grid spacings of 20 m. This suggests that like most LES representations of cloudy boundary layers, our results have likely not reached strict numerical convergence. However, the results are within the realm of the MC3E observations as established in Mechem et al. (2015), giving us confidence in their reasonableness. Previously, the authors reported little sensitivity to domain size for this case. We refer the reader to Mechem et al. (2015) for additional details about the model.

Instead of the size-resolving (bin) microphysics used in Mechem et al. (2015), for reasons of computational expense we employ the two-moment bulk parameterization of Morrison et al. (2005). The warm-rain component uses the autoconversion formulation of Khairoutdinov and Kogan (2000), which is slightly different from the original formulation of autoconversion in Morrison et al. (2005) that employed the scheme of Beheng (1994). As in Mechem et al. (2015), we assume a specified cloud condensation nuclei (CCN) concentration

of 425 cm^{-3}, which corresponded to a mean CCN concentration directly measured at SGP over a period from 0600 to 2000 UTC (at supersaturation $S = 0.47\%$). The behavior of the domain-mean accumulated surface precipitation for the bulk-microphysics control simulation (1.37 mm) compares favorably to the comparable bin-microphysics simulation in Mechem et al. (2015) (1.17 mm; Figure 8 and Tables 2 and 3 in Mechem et al., 2015), justifying the use of bulk microphysics in our comparison. Model-generated precipitation area fraction, as delineated by the area of radar reflectivity greater than 30 dB*Z*, is somewhat smaller than in the bin case, suggesting stronger conditionally sampled rain rates.

For simplicity, all simulations employed specified, horizontally homogeneous, time-varying surface fluxes from the ARM variational analysis product as in Mechem et al. (2015). (The version of SAM we used was not equipped with a land surface parameterization.) Previous research has demonstrated that horizontal inhomogeneity in surface properties (e.g., land use categories and soil moisture) can have an influence on boundary layer properties (e.g., Brunsell et al., 2011) and on the shallow-to-deep transition (Cioni & Hohenegger, 2017; Wu et al., 2015). However, in this case, we surmised that the transition was brought about by large-scale advective tendencies, as opposed to surface fluxes, which in this case were rather modest given the time of year (maximum surface sensible and latent heat fluxes of ~170 and ~200 W m^{-2}, respectively). Sensitivity simulations (not shown) varying the surface fluxes of both heat and moisture by ±25% resulted in nearly imperceptible changes to precipitation onset time and transition behavior and differences in accumulated precipitation much less than 25%. Although not directly evaluating the importance of representing horizontal heterogeneity, the lack of strong sensitivity to substantial changes in surface fluxes suggests that accounting for heterogeneity is probably unnecessary in this particular case.

All simulations used the semidiagnostic framework wherein the model is forced from observationally derived fields that are calculated using the variational analysis. Our control simulation setup is equivalent to the 1200v_75 simulation from Mechem et al. (2015), which imposes a time-varying forcing from the 75 km variational analysis domain beginning at 1200 UTC. Given the many challenges of this case (transient in time and nonhomogeneous in space), the simulations in Mechem et al. (2015) forced with this product performed admirably in representing many aspects of the transient cloud behavior. We noted that simulated precipitation onset was too early, however, and the precipitation rate was too strong. It was concluded that this was likely because the forcing was too destabilizing, from either excessive moisture advection or overly rapid destabilization of the temperature profile. We noted that the simulations are also sensitive to the imposed large-scale vertical motion, with changes of ±25% producing ~30 min shifts in precipitation onset and ~20% differences in accumulated precipitation. We say this to emphasize the importance of quality forcing data sets but do not further explore the sensitivity to large-scale vertical motion.

Although one could simply reduce or otherwise modify the forcing terms, how best to modify the forcing profiles is not obvious. This study chooses to relax the thermodynamic profiles to the observed MC3E profiles as captured in the variational analysis rather than reducing the forcing directly. The relaxation approach is particularly justified because the forcing terms at the 75 km scale are dominated by the RUC model output (Rapid Update Cycle) (Benjamin, Dévényi, et al., 2004; Benjamin, Grell, et al., 2004) used in the variational analysis method (Zhang & Lin, 1997), which heavily weights the Central Facility sounding (proximity) and is influenced weakly by the soundings at the SGP boundary facilities. Applying relaxation at various timescales corresponds to reducing the forcing by varying degrees. We perform a suite of simulations relaxing the moisture profile, temperature profile, and then both profiles, across a number of timescales (1, 2, 3, 5, and 9 h), for a total of 16 simulations. We then quantify the degree to which this relaxation reduces the forcing imposed by the variational analysis terms. The amount of this relaxation required suggests substantial error that may arise from a number of sources, with possibilities including model structural error (e.g., physical parameterizations); a violation of the scale separation assumption between the scale range resolved by the LES and the large-scale forcing terms; and uncertainty in the variational analysis product, which may include a mismatch between the forcing terms and the state variables (thermodynamic profiles).

4. Simulation Results: Control and Optimal Observational Metric Runs

In addition to our control simulation for the 25 May 2011 event, 15 sensitivity runs were performed, with each run characterized by different relaxation formulations. Relaxation was applied to the temperature and moisture fields (*TQ*), as well as separate runs for relaxation only for the temperature field (*T*-only) and the moisture

Table 1
Summary of Simulation Results From the Early Period of the Simulation (3–6 h)

Simulation name	CF	CT height (km)	Precipitation onset time (h)	Precipitation area fraction	Precipitation (mm)
Control	0.54 (0.57)	1.55 (1.53)	5.4	0.002–0.007 (<0.01)	0.06
tau = 1 h, *TQ*	<0.01	0.99 (0.98)	-	<0.001 (<0.001)	0.00
tau = 2 h, *TQ*	0.03 (0.02)	1.00 (0.99)	-	<0.001 (<0.001)	0.00
tau = 3 h, *TQ*	0.13 (0.11)	1.06 (1.04)	-	<0.001 (<0.001)	<0.01
tau = 5 h, *TQ*	0.27 (0.30)	1.18 (1.14)	7.2	<0.001 (<0.001)	<0.01
tau = 9 h, *TQ*	0.39 (0.43)	1.31 (1.26)	6.8	<0.001 (<0.001)	0.01
tau = 1 h, *T* only	0.09 (0.05)	0.93 (0.87)	8.3	<0.001 (<0.001)	<0.01
tau = 2 h, *T* only	0.22 (0.22)	1.17 (1.12)	7.1	<0.001 (<0.001)	<0.01
tau = 3 h, *T* only	0.29 (0.32)	1.26 (1.19)	7.6	<0.001 (<0.001)	<0.01
tau = 5 h, *T* only	0.37 (0.40)	1.36 (1.32)	6.6	0.000–0.001 (<0.001)	0.01
tau = 9 h, *T* only	0.45 (0.48)	1.42 (1.40)	5.9	0.000–0.002 (<0.001)	0.01
tau = 1 h, *Q* only	0.31 (0.27)	1.13 (1.12)	7.0	<0.001 (<0.001)	<0.01
tau = 2 h, *Q* only	0.39 (0.41)	1.19 (1.16)	6.3	<0.001 (<0.001)	<0.01
tau = 3 h, *Q* only	0.43 (0.48)	1.26 (1.22)	6.2	<0.001 (<0.001)	<0.01
tau = 5 h, *Q* only	0.48 (0.53)	1.34 (1.30)	6.1	<0.001 (<0.001)	0.01
tau = 9 h, *Q* only	0.51 (0.57)	1.42 (1.40)	5.9	0.000–0.002 (<0.001)	0.01

Note. Data columns represent mean cloud fraction (median in parentheses), median cloud top height (90th percentile height in parentheses), precipitation onset time (defined as the time when the surface precipitation rate first reaches the threshold value of 1 mm d^{-1}), mean and median precipitation area fraction (area fraction of 30 dB*Z* echo), and total precipitation accumulated over the 3 h period.

field (*Q*-only). The actual model thermodynamic variables are liquid water static energy (proportional to liquid water potential temperature) and total water, but for simplicity we refer to relaxing the temperature and moisture fields. The full suite of runs is summarized in Tables 1 and 2. Similar to Mechem et al. (2015), simulation behavior over the early-event period (3–6 h time interval; 1500–1800 UTC) and late-event period (6–9 h time interval; 1800–2100 UTC) is provided. For each series of runs (*TQ*, *T*-only and *Q*-only), reducing the forcing timescale corresponds to a stronger correction of the forcing toward the observational profiles (as reflected in the variational analysis product). The shorter relaxation timescales lead to later precipitation onset and weaker precipitation. We interpret this to be the result from a reduction in the destabilization from the large-scale forcing, which we will demonstrate in section 5. Because precipitation rate is loosely proportional to cloud depth, it is unsurprising that the shorter relaxation timescale runs that produce shallower clouds also have less precipitation.

Table 2
Summary of Simulation Results From the Late Period of the Simulation (6–9 h)

Simulation name	CF	CT height (km)	Precipitation onset time (h)	Precipitation area fraction	Precipitation (mm)
Control	0.73 (0.70)	2.81 (3.14)	5.4	0.031–0.059 (0.031–0.059)	1.31
tau = 1 h, *TQ*	0.02 (0.01)	1.06 (1.05)	-	<0.001 (<0.001)	0.00
tau = 2 h, *TQ*	0.26 (0.27)	1.29 (1.28)	-	<0.001 (<0.001)	<0.01
tau = 3 h, *TQ*	0.47 (0.49)	1.57 (1.51)	-	<0.001 (<0.001)	0.01
tau = 5 h, *TQ*	0.67 (0.69)	2.08 (2.13)	7.2	0.006–0.015 (0.004–0.009)	0.22
tau = 9 h, *TQ*	0.78 (0.79)	2.43 (2.62)	6.8	0.015–0.035 (0.018–0.048)	0.59
tau = 1 h, *T* only	0.53 (0.58)	1.72 (1.71)	8.3	0.003–0.007 (0.002–0.007)	0.09
tau = 2 h, *T* only	0.60 (0.63)	2.01 (2.08)	7.1	0.008–0.018 (0.006–0.017)	0.24
tau = 3 h, *T* only	0.71 (0.74)	2.17 (2.29)	7.6	0.005–0.015 (0.002–0.008)	0.16
tau = 5 h, *T* only	0.75 (0.76)	2.42 (2.63)	6.6	0.013–0.032 (0.012–0.029)	0.50
tau = 9 h, *T* only	0.70 (0.75)	2.61 (2.89)	5.9	0.026–.053 (0.031–0.057)	1.01
tau = 1 h, *Q* only	0.85 (0.86)	2.30 (2.46)	7.0	0.015–0.035 (0.006–0.022)	0.45
tau = 2 h, *Q* only	0.80 (0.79)	2.48 (2.69)	6.3	0.020–0.045 (0.019–0.051)	0.78
tau = 3 h, *Q* only	0.81 (0.85)	2.56 (2.81)	6.2	0.022–0.047 (0.018–0.046)	1.02
tau = 5 h, *Q* only	0.83 (0.88)	2.66 (2.92)	6.1	0.026–0.053 (0.024–0.046)	1.03
tau = 9 h, *Q* only	0.77 (0.81)	2.80 (3.14)	5.9	0.032–0.059 (0.025–0.060)	1.46

Note. Data columns represent mean cloud fraction (median in parentheses), median cloud top height (90th percentile height in parentheses), precipitation onset time (defined as the time when the surface precipitation rate first reaches the threshold value of 1 mm d^{-1}), mean and median precipitation area fraction (area fraction of 30 dB*Z* echo), and total precipitation accumulated over the 3 h period.

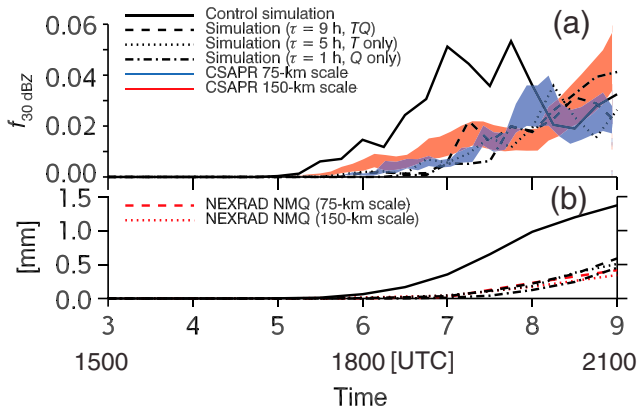

Figure 3. (a) Time series of echo fraction from the C-SAPR and four of the simulations. The width of the C-SAPR time series corresponds to precipitation area defined according to thresholds of 25 and 30 dB*Z*. The black line represents the control simulations, and the dashed, dotted, and dash-dotted lines represent sensitivity simulations chosen to best match the observations of accumulated rainfall shown in (b). The 9 h, *TQ* simulation indicated by the dashed line, representing a relaxation a timescale of 9 h of both the temperature and moisture profiles as described in the first paragraph of section 4. The *T*-only (dotted line) and *Q*-only (dash-dot line) simulations relax only those variables at the indicated timescale. (b) Accumulated precipitation from the simulations and the NEXRAD NMQ observational estimate.

Results from a number of simulations that best matched the observed precipitation totals and onset times (herein, collectively referred to as "optimal") are shown in Figure 3. These simulations were identified visually as good matches with the observed precipitation properties (Figure 3) and from the error statistics in Table 3. For the *TQ* runs, this optimal performance was achieved using a 9 h relaxation. A similar performance was achieved with a 5 h relaxation for the *T*-only runs and 1 h relaxation for the *Q*-only runs. Our discussion throughout the rest of the paper will focus on the control simulation and these three optimal sensitivity simulations. The upper panel shows the areal fraction coverage occupied by precipitation, which indicates regions occupying radar reflectivity factors greater between 25 dB*Z* and 30 dB*Z* (to allow for a range of radar measurement uncertainty in light-rain conditions, as in Mechem et al., 2015). The lower panel confirms the agreement between NEXRAD-based precipitation totals at different spatial scales and our selected runs. In comparison to the control run, these simulations exhibit improved performance, albeit this result is unsurprising since these runs were selected on the basis of improvements in the total domain precipitation and onset timing. The observed agreement with the 75 km and 150 km scale areal precipitation echo coverage (>30 dB*Z*) is encouraging. This is because a similar spatial rainfall topology and evolution is not guaranteed even if onset and total precipitation characteristics are matched. The *Q*-only runs exhibit the lowest areal fraction coverage for an extended period, but all runs are consistent with the observations if judged by our conservative spread for radar-based estimate uncertainty (e.g., radar miscalibration and sampling errors) in precipitation coverage.

Although we do not emphasize cloud fraction CF as means to diagnose model pathologies in this study, values for these newly prioritized runs are found in better agreement with the multisensor retrievals first shown in Mechem et al. (2015). Overall, Mechem et al. (2015) suggested that CF estimates from various observational methodologies (as well as previous simulations) were noisy. Since CF estimates were not anticipated

Table 3
Absolute and Relative Errors for Simulation-Calculated Total Accumulated Precipitation and 6–9 h Mean 30 dBZ Echo Area Fraction, Relative to Values Calculated From the MC3E Observations

	Error in total accumulated precipitation		Error in 30 dBZ echo area fraction	
Simulation name	Absolute error (mm)	Relative error (%)	Absolute error (fraction)	Relative error (%)
Control	0.95	228.8	0.021	211.1
tau = 1 h, *TQ*	−0.42	−100.0	−0.010	−100.0
tau = 2 h, *TQ*	−0.42	−100.0	−0.010	−100.0
tau = 3 h, *TQ*	−0.41	−98.6	−0.010	−99.3
tau = 5 h, *TQ*	−0.20	−47.1	−0.004	−38.6
tau = 9 h, *TQ*	**0.17**	**41.4**	**0.005**	**47.3**
tau = 1 h, *T* only	−0.33	−79.5	−0.007	−66.6
tau = 2 h, *T* only	−0.18	−43.0	−0.002	−18.1
tau = 3 h, *T* only	−0.26	−61.3	−0.005	−48.2
tau = 5 h, *T* only	**0.09**	**21.9**	**0.003**	**35.2**
tau = 9 h, *T* only	0.61	145.0	0.016	160.5
tau = 1 h, *Q* only	**0.03**	**8.3**	**0.005**	**51.0**
tau = 2 h, *Q* only	0.36	87.4	0.010	105.5
tau = 3 h, *Q* only	0.61	145.7	0.012	124.3
tau = 5 h, *Q* only	0.62	148.9	0.016	157.2
tau = 9 h, *Q* only	1.05	251.9	0.022	218.7

Note. The observed accumulated precipitation estimate obtained from the 75 km NEXRAD NMQ product is 0.42 mm, and the observed mean area fraction of the 30 dB*Z* echo is 0.0099 (CSAPR, 75 km scale). The three optimal simulations discussed in the paper are boldfaced. Note that the relative error of the 2 h, *T*-only simulation was −18.1%, which was smaller than the simulation we chose (5 h, *T*-only), but we prioritized picking simulations with the smallest precipitation error.

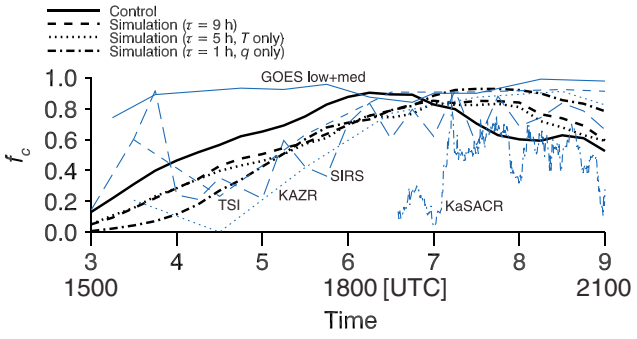

Figure 4. Five observational estimates of cloud fraction, all denoted by (bottom) blue lines overlaid on cloud fraction calculated from the simulation suite. The black line represents the control (1200v_75) simulation. Adapted from Mechem et al. (2015). Precipitation onset at the ARM SGP CF as based on collocated rain gauge was at 1920 UTC. Adapted from Mechem et al. (2015).

to be a reliable metric based on previous studies, there is cautious optimism when reporting that optimal runs highlighted in Figure 4 found consistent CF behaviors with the gradual increases over time and ranges reported by ARM sensors (~0.70–0.85) during the transition period from shallow cumulus to congestus from ~1800 to 1900 UTC, as evident in Figure 5. The exact reason for this improved cloud-fraction behavior is difficult to discern, however.

Figure 5a plots observed cloud coverage in terms of the frequency of occurrence of the highest cloud top, in this example estimated by the vertically pointing KAZR. Averaged hydrometeor fraction from ARSCL products is also plotted for the event (Figure 5b). These observations illustrate the timing of the cloud field deepening and its bimodal structure, as summarized by Borque et al. (2014) for scanning radar observations. Figure 6 plots the corresponding cloud top distribution from the optimal LES runs and the control run. Relative to the control run, the optimal simulations delay precipitation onset by 1–1.5 h, aligning better with the observed precipitation onset timing (~1900 UTC from the disdrometer at the SGP CF; see Figure 3b in Mechem et al., 2015). Figures 5 and 6 indicate that all simulations faithfully capture important time-varying aspects of the bimodal cloud top distribution found in observations. In contrast to previous Mechem et al. (2015) examples, the optimal simulations are in better alignment (slightly underestimate) with the height of this congestus mode as compared to ARM radar observations. Morphological differences are still visible between these runs, for example, when comparing the 1 h *Q*-only simulation to the other optimal runs. In particular, the 1 h *Q*-only run considerably delays cloud field deepening (in line with the initial reduction in areal precipitation coverage). However, when the congestus develop, this simulation overestimates the frequency of occurrence for congestus cloud tops relative to other optimal runs. In this sense, the 1 h *Q*-only simulation is less consistent with the observed, commingled shallow and congestus behaviors.

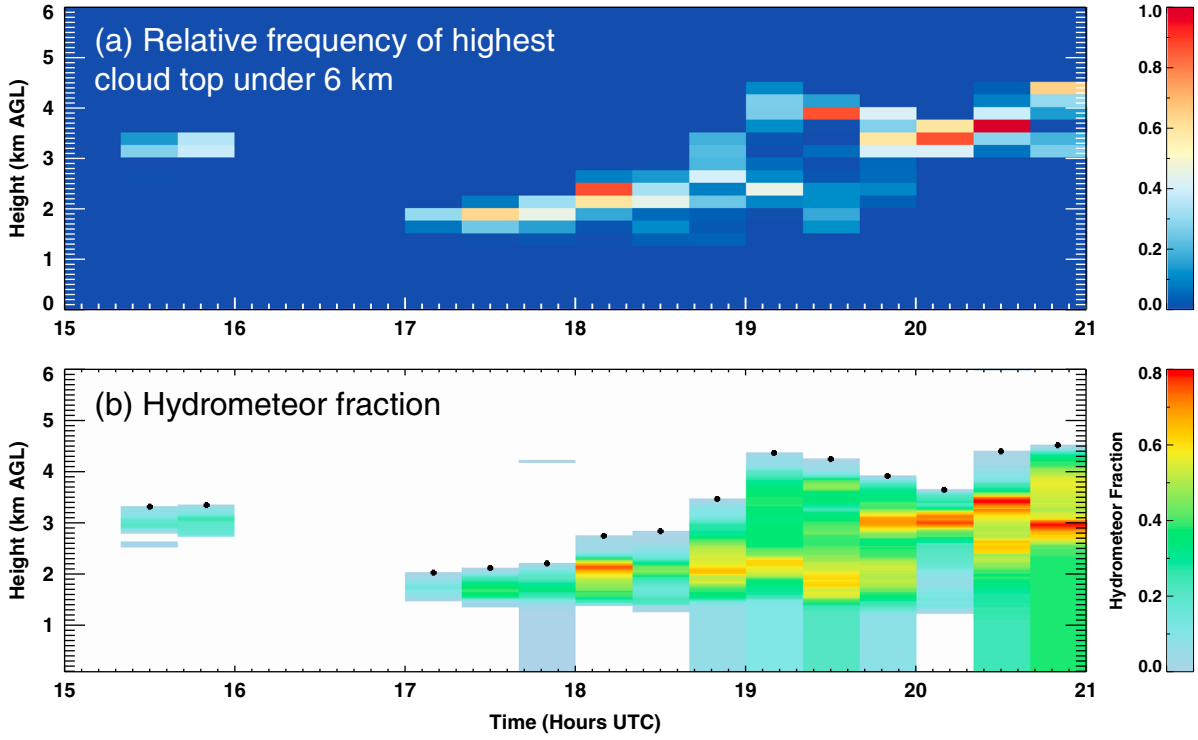

Figure 5. (a) Frequency of occurrence of highest cloud top under 6 km, calculated from KAZR-ARSCL cloud top product and binned in intervals of 20 min in time and 250 m in the vertical. (b) Time-height section derived from KAZR-ARSCL of hydrometeor fraction, averaged over 20 min intervals, overlaid with cloud top (black dots). Adapted from Mechem et al. (2015).

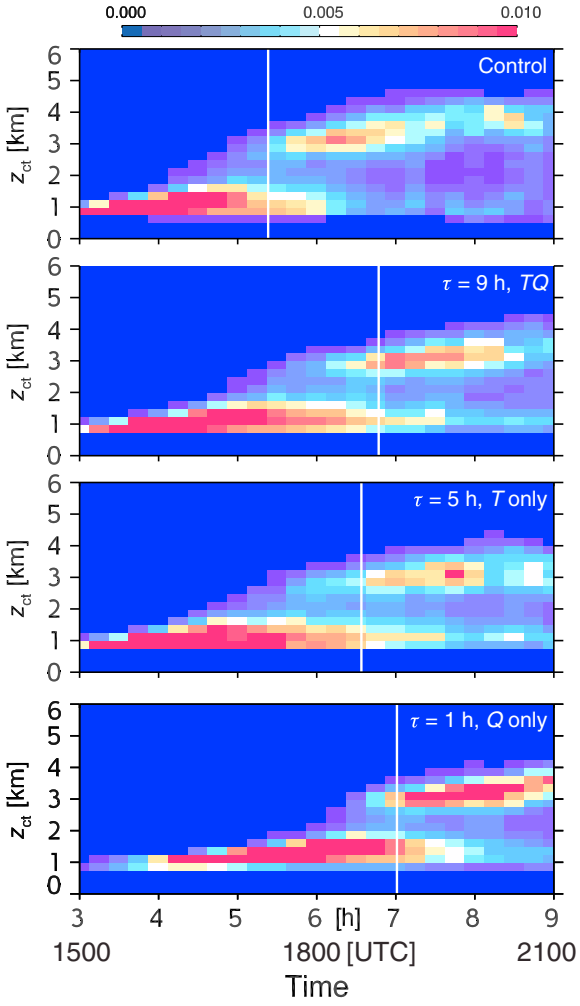

Figure 6. Cloud top height probability density functions (PDFs) for the control simulation and the three sensitivity experiments that best match the observed accumulated precipitation. The white vertical lines represent precipitation onset time, taken to be the threshold surface precipitation rate of 1 mm d^{-1}.

Figure 7 plots the differences in cloud system evolution between the control simulation and two of the optimal simulations (9 h *TQ* and 1 h *Q*-only; the 5 h *T*-only simulation was omitted because of its similarity to the 9 h *TQ* run), viewed in terms of the cross sections for radar reflectivity factor *Z*. The figure panels show that the control simulation produces precipitating congestus cells as early as 1700 UTC. Over the next 2 h, the cells rapidly increase in strength and coverage. By 1900 UTC, the domain contains two to three large precipitating congestus cells. The 9 h *TQ* optimal simulation reflects a delay in the transition to precipitating cells (~1800 UTC), and cloud coverage increases from 1800 to 1900 UTC, consistent with scanning radar behaviors. The 1 h *Q*-only simulation appears slower to develop congestus cells, with substantial congestus coverage occurring just prior to 1900 UTC. Congestus cells in the two optimal simulations also appear weaker in precipitation intensity (e.g., lower *Z*) and less organized when compared to the control simulation.

5. Simulation Results: Thermodynamic/Stability Behaviors for Control/Optimal Runs

The previous section highlights optimal runs as those providing reasonable depictions for the 25 May 2011 cloud transition across a variety of ARM macroscale cloud observational metrics and potentially offering a significant improvement over a baseline time-varying forcing simulation. Mechem et al. (2015) speculated that the cloud transitions for this event were predominantly governed by changes in low-level stability, based on the analysis of both steady state and time-evolving forcing data set behaviors. We acknowledge that evaporatively driven cold pools may also play a role in the transition and mesoscale organization of clouds (see the survey article by Zuidema et al., 2017). Our simulations that produce precipitation also yield cold pools, but we felt that an analysis of the transition from the perspective of cold pools was beyond the scope of the article. This section investigates the role of the evolution of stability profiles for the control and optimal simulations in governing the transition from shallow cumulus to congestus.

5.1. Thermodynamic Profile Behaviors

The large-scale tendency profiles in Figure 8 are provided for this event as initial justification for the role advection of temperature and moisture should play in the transition from shallow cumulus to congestus. The horizontal advection of the potential temperature (Figure 8, top row) over the 1200–1400 UTC period indicates predominantly cold air advection from the surface to ~4 km, which extends upward after 1400 UTC. A uniform and negative advection profile would be destabilizing for a surface-based parcel; however, this constant advection profile would not modify the potential temperature profile lapse rate. Advection profiles that become more negative with height (e.g., as observed between 1 and 2.5 km at 1600 UTC or between 2 and 2.5 km at 1800 UTC) will formally destabilize the layer. In that regard, destabilization of these elevated layers may govern the more rapid transition from shallow to congestus clouds.

As just mentioned, a constant layer of cold advection may also destabilize the layer for a warm, surface-based parcel. This path is plausible given the nonnegligible surface heat and moisture fluxes found for this case (see the flux time series in Figure 2 of Mechem et al., 2015). Additional forcing terms associated with our relaxation methods are positive (Figure 8, top row) and act to reduce the magnitude of destabilization relative to the control run. The moisture advection profiles indicate strong low-level moistening below 1.5 km; this moistening of the lower layer is in line with increasing CAPE (convective available potential energy) or moist static energy ($h = c_pT + gz + L_vq_v$). The magnitude of the relaxation terms (dashed lines in the lower row of Figure 8) suggests that the control simulation moisture advection is too strong when compared to the optimal simulations.

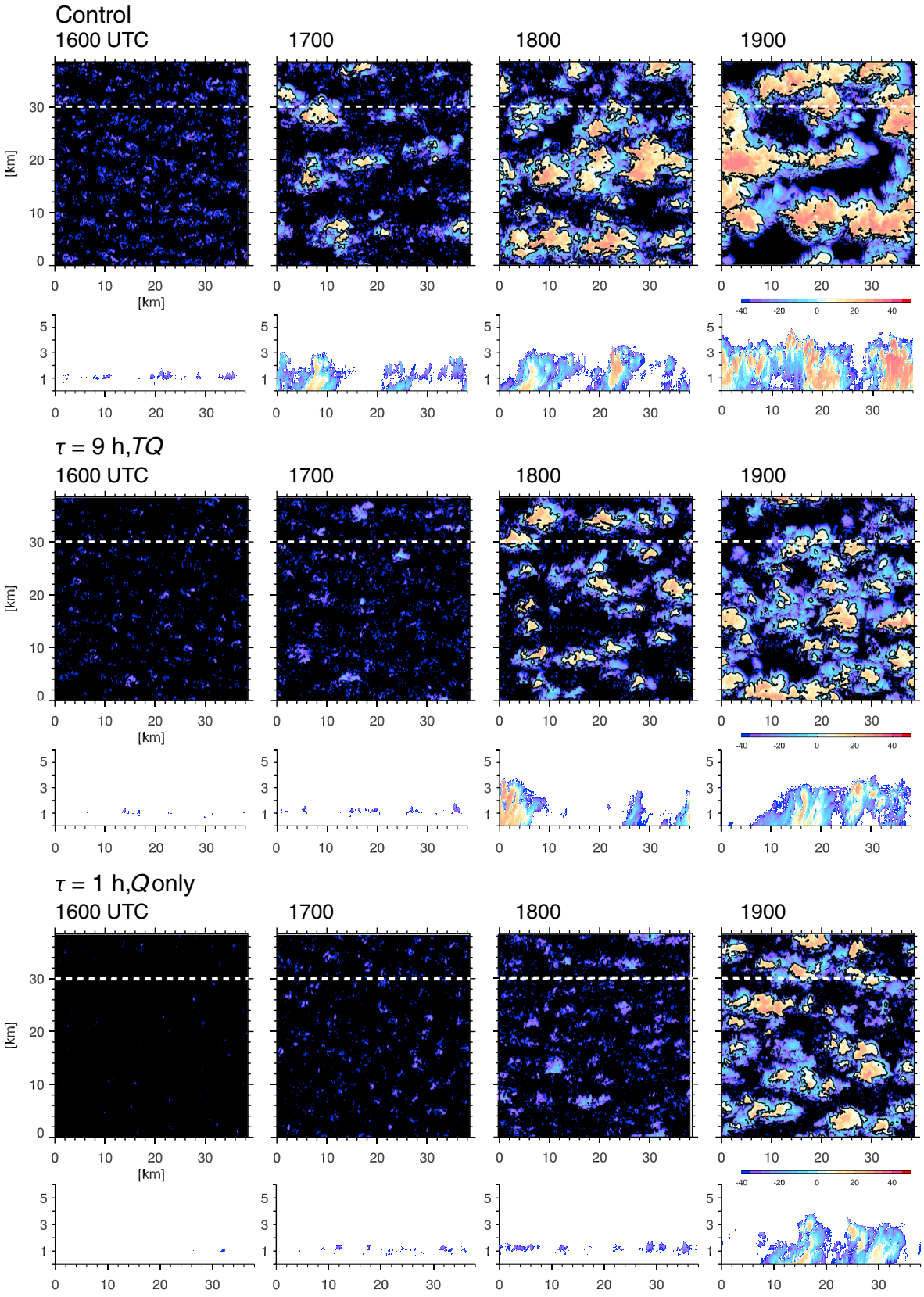

Figure 7. Time series of horizontal (altitude of 0.975 km) and vertical cross sections of simulated reflectivity from the control simulation. Vertical cross sections are taken through the regions designated by the dashed white lines.

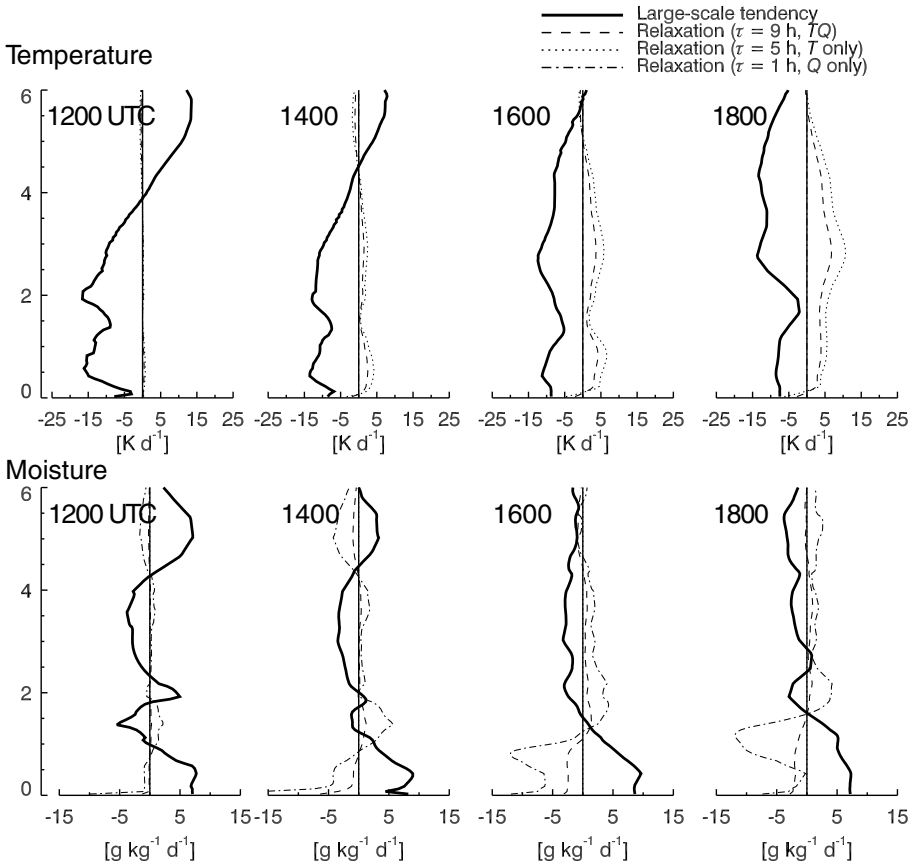

Figure 8. Profiles of the large-scale tendency of liquid water potential temperature and total water, along with relaxation rates for the three optimal simulations. Note that in the relaxation simulations, the total forcing is the sum of the large-scale tendency and the relaxation term.

The controls on the transition for the 25 May 2011 event are next viewed from the perspective of equivalent potential temperature (θ_e) profiles and their evolution (Figure 9, top row), having separate contributions from the potential temperature (θ, Figure 9, middle row) and total water mixing ratio (q_t, Figure 9, bottom row). Note that we use water vapor mixing ratio (q_v) rather than total water (q_t) to compute θ_e in these plots, given that areal means of the two quantities vary little. Figure 9 shows profiles from the control and optimal simulations, with gray regions in the figure panels indicating the spread of our entire simulation suite (i.e., all 16 simulations summarized in Tables 1 and 2). The observations are also overplotted, as reported by the ARM merged radiosonde product (e.g., Atmospheric Radiation Measurement (ARM) Climate Research Facility, 2001) and continuous variational analysis product.

For all simulations in Figure 9, θ_e profiles below 3 km trend more convectively unstable with time (e.g., the $d\theta_e/dz$ becomes more negative with time). The observationally derived θ_e profiles also exhibit this behavior, although to a lesser degree compared to the simulations. In particular, the simulations reduce θ_e at midlevels (~3 km) by as much as 2–4 K more relative to the observations. Nevertheless, the optimal simulations show a slight improvement over the control simulation, even though all simulations share the persistent low bias in midlevel θ_e. The temporal variation in θ_e over the lowest 1 km also differs substantially (~4 K) across these simulations. The potential temperature profiles (Figure 9, middle row) and total water (Figure 9, bottom row) help to isolate the temperature and moisture contributions to the θ_e variations. The most noticeable feature from the potential temperature profile evolution is that by 1800 UTC; all simulations are cooler (~1–3 K) than the ARM observations. Moreover, differences in stability identifiable by the potential temperature profiles over the duration of the simulations are not obvious. However, the evolution of the moisture profiles (especially over the lowest 1 km) is visibly different across the simulations. From 1600 to 1800 UTC, most simulations exhibit greater moisture relative to the observations. One exception to this behavior is the 1 h *Q*-only optimal run that is the most strongly relaxed to the observed moisture profiles.

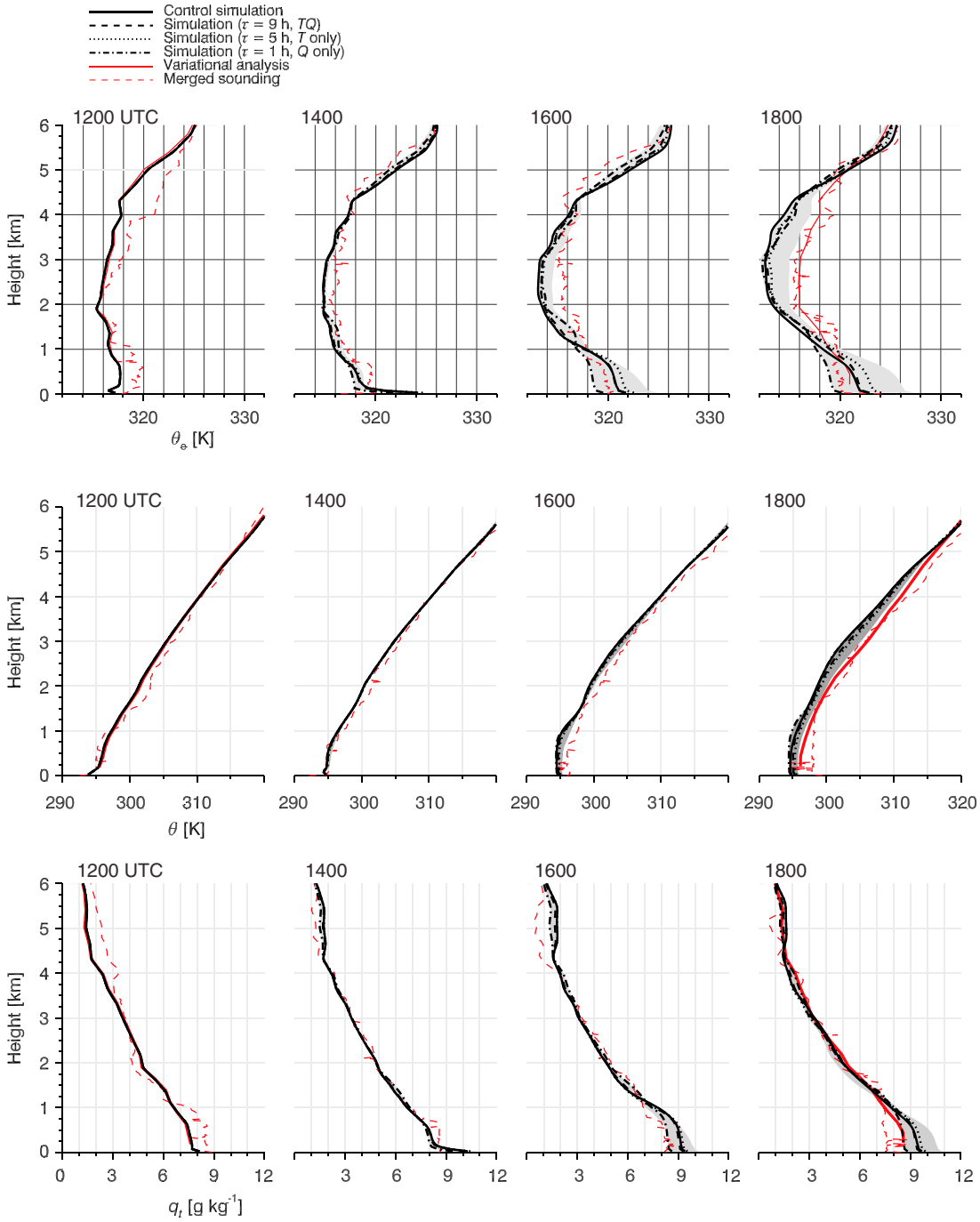

Figure 9. Vertical profiles of equivalent potential temperature, potential temperature, and total water mixing ratio as a function of time from the ARM variational analysis, merged sounding product, and SAM. The gray band represents the span of the entire model ensemble.

The analysis of Figure 9 suggests that midlevel temperature, as well as temperature and moisture over the lowest 1 km, may play a role in governing the transition for this event. The similarity of the moisture profiles above 1 km suggests that the moistening-deepening entrainment mechanism often active in shallow convection (Bretherton et al., 2005) does not explain the differences across the simulation suite. Figure 10 more closely explores the evolution of the observations, the control simulation, and the three optimal simulations. The figure plots the evolution of domain-mean profiles of θ_e and saturation equivalent potential temperature (θ_{es}). Overlaid on the profiles are parcel paths corresponding to parcels originating with mean thermodynamic properties over the lowest 500 m of the atmosphere, which are conserved under moist

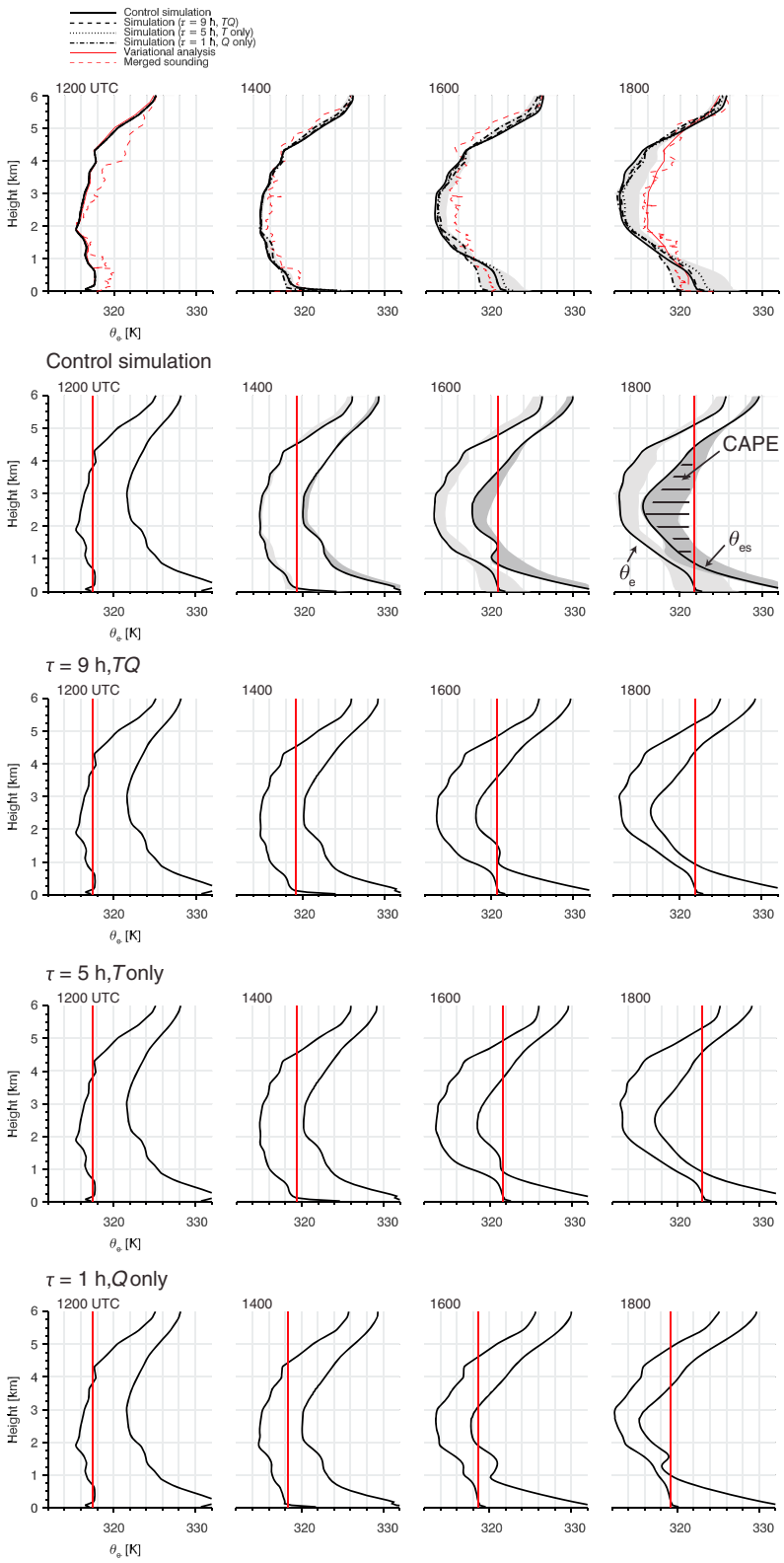

Figure 10. Vertical profiles of equivalent potential temperature and saturation equivalent potential temperature as a function of time from the ARM variational analysis, merged sounding product, and SAM. The gray band represents the span of the entire model ensemble. The solid red lines in the simulation profiles represent a parcel with mean properties from the lowest 500 m of the atmosphere. The top row shows the optimal simulations and the envelope that includes the entire ensemble and is equivalent to the top row in Figure 9.

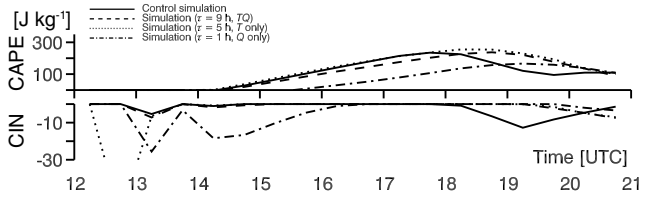

Figure 11. Time series of CAPE and CIN for the control simulation and three optimal simulations. CAPE and CIN calculations assume mean parcel properties over the lowest 500 m of the atmosphere. Note that the *y* axis scales of the CAPE and CIN time series are different.

adiabatic ascent. In this perspective, areas lying between the parcel path and the θ_{es} profile as denoted in the 1800 UTC control simulation panel in Figure 10 correspond to the CAPE. The four control simulation panels from 1200 to 1800 UTC show the evolution of the instability over that period. The profiles at 1200 and 1400 UTC indicate no instability, although they exhibit indications of destabilization. The 1600 UTC profile does show a small amount of CAPE, which increases substantially by 1800 UTC. Two of the three optimal simulations exhibit a similar behavior. The 9 h *TQ* simulation and the 5 h *T*-only simulation do not differ substantially from the control simulation, with zero CAPE in both until the 1600 UTC profiles. The 1 h *Q*-only simulation contains very little CAPE until approximately 1800 UTC and less overall CAPE than the other simulations. The precipitation time series in Figure 3 and the cloud top behavior in Figure 6 indicate that these optimal simulations exhibit a slower transition to deeper precipitating cloud (relative to the control simulation), yet this slower transition is not obvious in the Figure 10 thermodynamic profiles, except for the 1 h *Q*-only simulation, which develops CAPE much more slowly than the other simulations. This finding is confirmed in the time series of CAPE and convective inhibition (CIN) for the four simulations in Figure 11. All the simulations indicate increasing CAPE values over time (from ~1400 UTC onward), but the CAPE in the 1 h *Q*-only simulation becomes nonzero ~1.5 h later than in the other simulations. In the 1400–1600 UTC interval, CIN is negligible in all the simulations except for the 1 h *Q*-only run. Given that these optimal runs better match the observed precipitation amount and onset time compared to the control simulation, the similarity in the thermodynamic profiles and CAPE/CIN behavior across the simulations (except for the 1 h *Q*-only run) is surprising. These results suggest that any signs indicating the transition from shallow cumulus to precipitating congestus in these simulations are not obvious from the environmental thermodynamic variables or from the mean thermodynamic profiles themselves.

Figure 12 explores the evolution of stability by breaking down the profiles of unsaturated static stability $d\theta/dz$ into four, 1 km layers in order to see whether subtle changes in shallow-layer stability can explain differences in cloud transition behavior. Because of their later transition and precipitation onset time, we would expect the optimal simulations to exhibit more stability relative to the control simulation. In the lowest (0.5–1.5 km) layer, only the 1 h *Q*-only simulation is markedly different in the time leading up to the cloud transition and precipitation onset (recall that the onset times for the different simulations are between 1700 and 1900 UTC). In the 1.5–2.5 km layer, two of the optimal simulations (9 h *TQ* and 5 h *T*-only) are slightly more stable from 1600 to 1800 UTC. During this time period, the 1 h *Q*-only simulation is actually more unstable, which runs counter to what we would have expected given the delayed precipitation onset in the 1 h *Q*-only simulation. In the uppermost layer (3.5–4.5 km), the optimal simulations are all, to varying degrees, more unstable than the control in the period leading up to precipitation onset. These individual layers do not show an obvious control of environmental stability on cloud transition and precipitation onset.

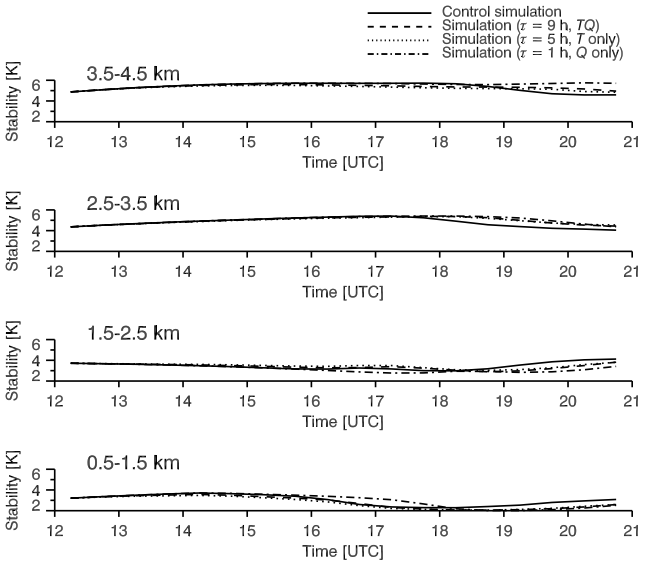

Figure 12. Unsaturated static stability of 1 km layers in the lower atmosphere. This is evaluated here simply as the change in potential temperature across the layer.

5.2. Cloud Buoyancy

The vertical profiles in Figures 9–12 indicate an atmosphere that is becoming more unstable over time and thus more conducive to congestus clouds. However, the traditional stability measures we have shown—vertical profiles, CAPE/CIN, or unsaturated static stability—are not able to clearly attribute differences in stability across the simulations to differences in observable ARM macroscale cloud properties including precipitation onset, areal fraction of precipitation, and cloud top height behavior. So what is driving the differences across the simulations?

The LES provides the opportunity to more closely explore the behavior of convection as the environment evolves over time. Wu et al.

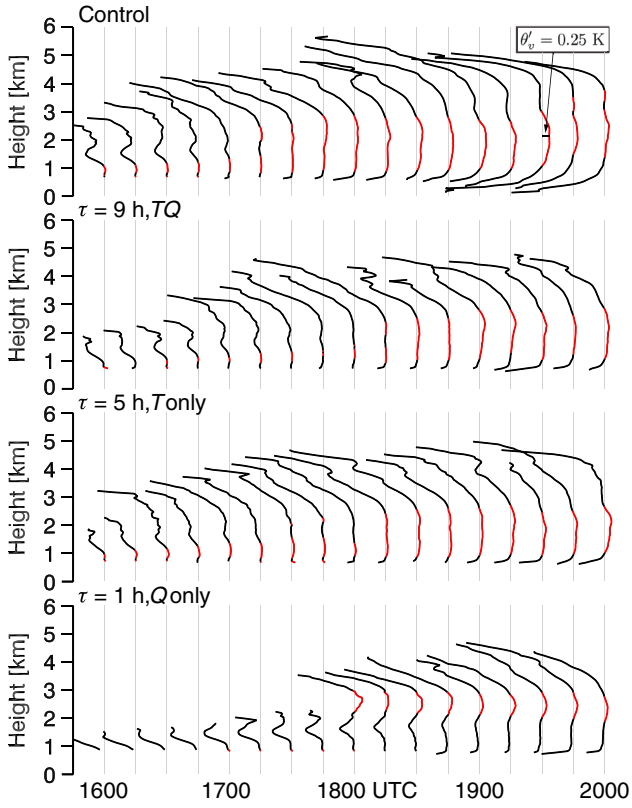

Figure 13. Time evolution (every 15 min) of horizontally averaged vertical profiles of virtual temperature excess for the control and three optimal simulations, obtained as the mean virtual temperature conditionally sampled in cloudy regions ($q_c > 0.01$ g kg^{-1}) minus the mean virtual temperature. The thin vertical gray lines indicate values of zero virtual temperature excess, and the red portions of the profile indicate positive values. The scale of the virtual temperature excess is indicated on the 1930 control simulation profile.

(2009) theorized that a cloud system transitions from shallow convection to deep, precipitating convection when the cloud elements, on average, become positively buoyant. Figure 13 shows the evolution of horizontally averaged vertical profiles of virtual temperature excess (θ_v', proportional to buoyancy and sometimes also referred to as "buoyancy excess") every 15 min for the control simulation and the three optimal simulations. In a manner consistent with Wu et al., here we define temperature excess as $\theta_v' = \theta_v - \overline{\theta}_v(z)$, that is, the mean virtual temperature (θ_v) conditionally sampled over all cloudy points ($q_c > 0.01$ g kg^{-1}, where q_c is cloud water mixing ratio) in a model level, minus the mean virtual temperature ($\overline{\theta}_v(z)$) of all the points in that level. The profiles then indicate layers of instantaneous positive and negative in-cloud buoyancy.

Early in the control simulation and prior to 1715 UTC, positive buoyancy (indicated by the red region of the profiles in Figure 13) is restricted to low levels, from just above cloud base to a height of about ~1.25 km. This corresponds to a thin layer of cumulus clouds, which are positively buoyant ("active" shallow cumulus, in the parlance of Zhang and Klein, 2013), which differs from the Wu et al. (2009) behavior where the shallow clouds are all negatively buoyant (the "forced" classification of Zhang and Klein, 2013). The shallow clouds remain shallow because of the strong negative θ_v' (again, proportional to buoyancy) at ~1.5 km. From 1600 to 1700 UTC, this negative θ_v' weakens, which is a result of the slow destabilization of that layer that can be seen in the 0.5–1.5 km layer in Figure 12. Eventually, the layer becomes sufficiently destabilized to allow the cloudy updrafts penetrating this layer to become positively buoyant again (1715 UTC onward). This transition to a deeper layer of positive buoyancy corresponds to a deepening in the cloud top PDFs in Figure 6.

Note that the profiles in Figure 13 and the cloud top PDFs in Figure 6 are not directly comparable. For example, during the early shallow period, Figure 13 may indicate a cloud buoyancy profile even for a single fortunate updraft with sufficient updraft strength to reach heights of 3–4 km. However, this behavior may not be a meaningful statistical contribution to the cloud field to show up in the cloud top PDFs in Figure 6. The development of positive in-cloud buoyancy over a deeper layer should be regarded as a diagnostic, as opposed to prognostic, indicator of the transition to deeper cloud. With this behavior in mind, however, the deepening of the positively buoyant layer may precede the transition of a large area of deepening cloud tops and then the onset of precipitation. In the control simulation, the deepening of the positively buoyant layer (Figure 13) corresponds well with the precipitation onset (Figure 6).

Unlike the more traditional stability metrics, the temperature excess profiles of the control and the optimal simulations differ. Positive buoyancy in the 9 h *TQ* and 5 h *T*-only simulations remains shallow until about 1815 UTC. This later transition relative to the control simulation corresponds well with the delayed transitions in cloud top and precipitation onset in Figure 6, although the transition in deepening positive cloud buoyancy slightly precedes the cloud top PDF transitions and precipitation onset for the reason discussed above. The combined behavior of the cloud top PDF, precipitation onset, and cloud buoyancy indicates that the 9 h *TQ* and 5 h *T*-only simulations are rather similar in behavior. However, the 1 h *Q*-only simulation differs substantially from the others. From 1600 to 1745 UTC, the shallow clouds are negatively buoyant, except right at cloud base. At 1800 UTC, an elevated layer of positive buoyancy from ~2 to 3 km develops, which is reflected in the cloud top PDFs (Figure 6). As with the other simulations, the development of this positive buoyancy precedes the precipitation onset (at 1900 UTC) and the development of prominent elevated cloud tops. This elevated layer of positive buoyancy contrasts substantially with the deep layer of positive buoyancy in the other simulations.

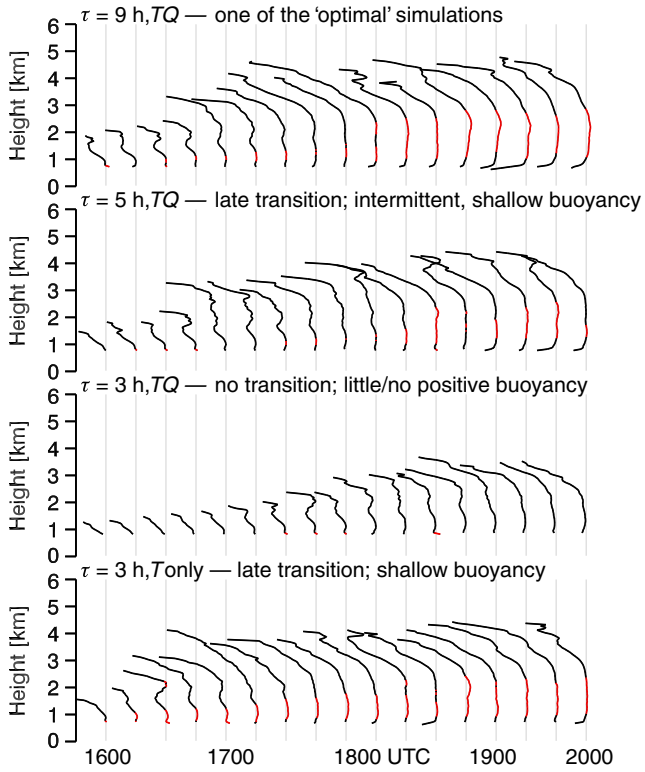

Figure 14. Time evolution (every 15 min) of horizontally averaged vertical profiles of virtual temperature excess, as in Figure 13, but for one of optimal simulations (top) and three poor simulations.

We contrasted the buoyancy behavior in one of the optimal runs (9 h *TQ*) with three selected poorly performing simulations (identified by poor precipitation onset times and total accumulated precipitation amounts), presented in Figure 14. We chose simulations only from the *TQ*- and *T*-only suites because even the best performing *Q*-only simulation was found to be substantially flawed, as previously discussed. From the perspective of evolving thermodynamic profiles, these simulations are not substantially different from the optimal simulations (not shown). Differences are apparent, however, in the virtual temperature excess (buoyancy) profiles in Figure 14. Compared to the optimal 9 h *TQ* simulation, the 5 h *TQ* simulation exhibits a late transition and a weaker (smaller θ_v'), somewhat shallow layer of positive buoyancy (1.3 versus 1.7 km). Moreover, the buoyancy behavior could best be described as intermittent, with a 1.4 km thick layer of positive buoyancy at 1845 UTC, very little positive buoyancy at 1900 UTC, and then positive buoyancy over a deeper layer returning afterward. The 3 h *TQ* simulation is worse, never developing the deep layer of positive buoyancy found in the 9 h *TQ* simulation. The buoyancy behavior in the 3 h *T*-only simulation is less intermittent than in the 5 h *TQ* run but nevertheless exhibits a late transition and a shallower layer of positive buoyancy relative to the optimal 9 h *TQ* simulation (1.2 versus 1.7 km). These profiles of virtual temperature excess show substantial differences between the optimal and poorly performing simulations. These profiles present the cloud-average view; deeper analysis might include exploring the cloud-sampled distributions θ_v' or joint distributions of θ_v' and vertical motion (*w*) as a function of height.

6. Discussion and Summary

In this study, we perform a suite of 16 simulations based on the 25 May 2011 MC3E event (Mechem et al., 2015), aimed at evaluating the controls on the transition from shallow cumulus to congestus, and the onset of surface precipitation. In order to better reproduce the observed behavior of precipitation onset and total precipitation, we relax the thermodynamic profiles (temperature, moisture, and both together) at selected timescales to the observed profiles from the ARM variational analysis product. From the full suite of simulations, three of the runs stood out as being optimal matches to the observed precipitation onset and total accumulation (9 h *TQ*, 5 h *T*-only, and 1 h *Q*-only) and performing notably better than the control simulation (Figure 4b). These three simulations also performed favorably for independent comparisons of cloud fraction (Figure 3), precipitation area fraction (Figure 4a), and evolution of cloud top PDFs (Figure 6). Overall, the 25 May 2011 case is characterized by substantial horizontal variability and rapid evolution and thus arguably represents a highly challenging case to attempt such simulations. Moreover, the combination of a traditional atmospheric LES approach (doubly periodic boundary conditions and statistically homogeneous) and horizontally averaged forcing profiles may not be fundamentally well posed for reproducing the complex spatiotemporal structure observed during this event. We acknowledge that this analysis focuses on a single case, and the generality of our findings should be explored over additional cases. Nevertheless, the SAM performed beyond expectations, with the optimal simulations (as with the control run, to a reasonable degree) capturing the salient aspects of this case as compared to a suite of macroscale cloud and precipitation observations.

Mechem et al. (2015) suggested that the shallow-to-congestus transition in this event was modulated by changes in environmental stability brought about by the large-scale forcing. Varying the relaxation timescale and the variable(s) being nudged changes the amount of forcing being applied in the model (Figure 8). Furthermore, by changing the thermodynamic profiles, we also likely influence the entrainment rate and cloud base mass flux (Grabowski et al., 2006), known to play roles in governing the transition from shallow to deep clouds. From the perspective of equivalent potential temperature (θ_e), we find that the observations and all of the simulations become less stable over time (Figure 9), with $d\theta_e/dz$ in the 0–3 km layer decreasing,

largely a result of cold advection increasing with height in the layer. Moisture advection contributes to increasing θ_e in the lowest 1 km. A closer look at profiles of θ_e and θ_{es} provides a parcel theory viewpoint and shows the evolution of CAPE relative to a parcel with mean properties from the lowest 500 m (Figure 10). As each of the simulations progress, CAPE becomes nonzero and is increasing over time. However, the profiles for the optimal simulations suggest little in the way of differences with the control simulation (except for the 1 h, *Q*-only run) that transitions too rapidly. A similar lack of clarity is provided in the time series of CAPE and CIN in Figure 11, with the control and two of the optimal simulations developing CAPE in a similar timeframe. Consulting the stability in 1 km deep layers (Figure 12) offers little additional insight. These figures demonstrate that all of the simulations exhibit destabilization over time but nonetheless suggest that we cannot discern differences in transitions from the environmental profiles alone.

With this limitation in mind, we explore conditionally sampled properties in the LES output fields. In a manner reminiscent of Wu et al. (2009), we find that the cloud transition from shallow to congestus occurs when the clouds become positively buoyant in the mean (Figure 13). Furthermore, this perspective of cloud behavior displays differences across the simulations. Namely, we find the delayed emergence of mean cloud buoyancy in two of the optimal simulations (9 h *TQ* and 5 h *T*-only) and the development of an elevated layer of positive buoyancy in the 1 h *Q*-only simulation. Although we do not have sufficient observations to evaluate which of these simulations is nearest to the truth, we speculate that the shallow, elevated layer of instability in the 1 h *Q*-only simulation is less physical, at least when compared to other studies that show conditionally sampled quantities from congestus (e.g., Figure 11 in Mechem & Oberthaler, 2013). This finding suggests that different simulations may be well matched to bulk observational statistics (e.g., observed precipitation behavior) but may take different paths to come to that solution, not all of which may be physically reasonable or consistent with other observational aspects of the case.

The challenge with evaluating cloud-core vertical air velocities from observations is well known given the sampling limitations associated with profiling and scanning cloud radars for basic cloud field properties (e.g., Oue et al., 2016). These factors include the limited areal coverage, sensitivity to clouds with range, and the low statistical probability of sampling the first-transitioning clouds. For this reason, and the even greater difficulty of high temporal resolution thermodynamic retrievals, it is unlikely that cloud buoyancy will be a practical macroscale observational metric obtained by ground radar observations for the foreseeable future.

The inability of the environmental profiles (alone) to discern subtle differences among the runs and the usefulness of conditionally sampled model quantities argues for hybrid observational/modeling approaches. These approaches include the recent LES ARM Symbiotic Simulation and Observation (Gustafson et al., 2017). Efforts of this sort promote a more holistic interpretation of an environment that destabilizes and undergoes convective overturning than do observations and parcel theory models alone. Our findings suggest that model output in these hybrid efforts should include cloud- and cloud-core sampled quantities (e.g., buoyancy) and fluxes. This work also recommends continued improvement of observationally constrained forcing data sets.

Acknowledgments
The authors are grateful to Marat Khairoutdinov for making SAM available to the scientific community. Observational data were obtained from the Atmospheric Radiation Measurement (ARM) Climate Research Facility, a U.S. Department of Energy (DOE) Office of Science user facility sponsored by the Office of Biological and Environmental Research. These data sets are directly found at the U.S. DOE SGP ARM Climate Research Facility (http://www.archive.arm.gov) website and the corresponding IOP websites for the Midlatitude Continental Convective Clouds Experiment (MC3E, http://campaign.arm.gov/mc3e/). Additional thanks to Shaocheng Xie (LLNL) for discussions on ARM continuous forcing products and to Michael Jensen (BNL) and Lucas McMichael (KU) for constructive comments on the manuscript. We greatly appreciate the thoughtful input from three anonymous reviewers. Some of the computing for this project was performed at the OU Supercomputing Center for Education and Research. Numerical simulation data will be archived at the NERSC (National Energy Research Scientific Computing Center, http://www.nersc.gov), a publically accessible repository for DOE-sponsored projects. Please contact the corresponding author (dmechem@ku.edu) for details. This research was supported by the Department of Energy Office of Science grants DE-SC0006736 and DE-SC0016522. Numerical simulation data are available on request of the corresponding author (dmechem@ku.edu), in accordance with AGU guidelines. This manuscript has also been authored by employees of Brookhaven Science Associates, LLC under contract DE-SC0012704 with the U.S. DOE. The publisher by accepting the manuscript for publication acknowledges that the United States Government retains a nonexclusive, paid-up, irrevocable, worldwide license to publish or reproduce the published form of this manuscript, or allow others to do so, for United States Government purposes.

References

Ackerman, A. S., van Zanten, M. C., Stevens, B., Savic-Jovcic, V., Bretherton, C. S., Chlond, A., et al. (2009). Large-eddy simulations of a drizzling, stratocumulus-topped marine boundary layer. *Monthly Weather Review*, *137*(3), 1083–1110. https://doi.org/10.1175/2008MWR2582.1

Atmospheric Radiation Measurement (ARM) Climate Research Facility (2001). updated hourly. Merged Sounding (MERGESONDE1MACE). 2001–04-01 to 2015–06-29, North Slope Alaska (NSA) Central Facility, Barrow AK (C1). Compiled by D. Troyan, S. Giangrande and T. Toto. Atmospheric Radiation Measurement (ARM) Climate Research Facility Data Archive: Oak Ridge, Tennessee, USA. Data set accessed 2017–04-18 at: https://doi.org/10.5439/1034922

Atmospheric Radiation Measurement (ARM) Climate Research Facility (2011a). updated hourly. Active Remote Sensing of CLouds (ARSCL) product using Ka-band ARM Zenith Radars (ARSCLKAZR1KOLLIAS). 2011–05-24 to 2011–05-25, Southern Great Plains (SGP) Central Facility, Lamont, OK (C1). Compiled by K. Johnson, S. Giangrande and T. Toto. Atmospheric Radiation Measurement (ARM) Climate Research Facility Data Archive: Oak Ridge, Tennessee, USA. Data set accessed 2017–04-19 at: https://doi.org/10.5439/1350629

Atmospheric Radiation Measurement (ARM) Climate Research Facility (2011b). updated hourly. Ka-Band Scanning ARM Cloud Radar (KASACRHSRHI). 2011–05-24 to 2014–07-31, Southern Great Plains (SGP) Central Facility, Lamont, OK (C1). Compiled by A. Matthews, B. Isom, D. Nelson, I. Lindenmaier, J. Hardin, K. Johnson and N. Bharadwaj. Atmospheric Radiation Measurement (ARM) Climate Research Facility Data Archive: Oak Ridge, Tennessee, USA. Data set accessed 2017–04-19 at: https://doi.org/10.5439/1046197

Atmospheric Radiation Measurement (ARM) Climate Research Facility (2011c). updated hourly. C-Band ARM Precipitation Radar (CSAPRSUR). 2011–05-24 to 2011–05-25, Southern Great Plains (SGP) Nardin, OK (C-band radar site, Intermediate / Auxiliary) (I7). Compiled by A. Matthews, B. Isom, D. Nelson, I. Lindenmaier, J. Hardin, N. Bharadwaj and S. Collis. Atmospheric Radiation Measurement (ARM) Climate Research Facility Data Archive: Oak Ridge, Tennessee, USA. Data set accessed 2017–04-19 at: https://doi.org/10.5439/1025170

Beheng, K. D. (1994). A parameterization of warm cloud microphysical conversion processes. *Atmospheric Research*, *33*(1-4), 193–206. https://doi.org/10.1016/0169-8095(94)90020-5

Benjamin, S. G., Dévényi, D., Weygandt, S. S., Brundage, K. J., Brown, J. M., Grell, G. A., et al. (2004). An hourly assimilation–forecast cycle: The RUC. *Monthly Weather Review*, *132*(2), 495–518. https://doi.org/10.1175/1520-0493(2004)132%3C0495:AHACTR%3E2.0.CO;2

Benjamin, S. G., Grell, G. A., Brown, J. M., Smirnova, T. G., & Bleck, R. (2004). Mesoscale weather prediction with the RUC hybrid isentropic–terrain-following coordinate model. *Monthly Weather Review*, *132*(2), 473–494. https://doi.org/10.1175/1520-0493(2004)132%3C0473:MWPWTR%3E2.0.CO;2

Bony, S., & Dufresne, J.-L. (2005). Marine boundary layer clouds at the heart of tropical cloud feedback uncertainties in climate models. *Geophysical Research Letters*, *32*, L20806. https://doi.org/10.1029/2005GL023851

Borque, P., Kollias, P., & Giangrande, S. (2014). First observations of tracking clouds using scanning ARM cloud radars. *Journal of Applied Meteorology and Climatology*, *53*(12), 2732–2746. https://doi.org/10.1175/JAMC-D-13-0182.1

Bretherton, C. S., Blossey, P. N., & Khairoutdinov, M. (2005). An energy-balance analysis of deep convective self-aggregation above uniform SST. *Journal of the Atmospheric Sciences*, *62*(12), 4273–4292. https://doi.org/10.1175/JAS3614.1

Brown, A. R., Cederwall, R. T., Chlond, A., Duynkerke, P. G., Golaz, J. C., Khairoutdinov, M., et al. (2002). Large-eddy simulation of the diurnal cycle of shallow cumulus convection over land. *Quarterly Journal of the Royal Meteorological Society*, *128*(582), 1075–1093. https://doi.org/10.1256/003590002320373210

Brunsell, N. A., Mechem, D. B., & Anderson, M. C. (2011). Surface heterogeneity impacts on boundary layer dynamics via energy balance partitioning. *Atmospheric Chemistry and Physics*, *11*(7), 3403–3416. https://doi.org/10.5194/acp-11-3403-2011

Cioni, G., & Hohenegger, C. (2017). Effect of soil moisture on diurnal convection and precipitation in large-eddy simulations. *Journal of Hydrometeorology*, *18*(7), 1885–1903. https://doi.org/10.1175/JHM-D-16-0241.1

Clothiaux, E. E., Ackerman, T. P., Mace, G. G., Moran, K. P., Marchand, R. T., Miller, M. A., & Martner, B. E. (2000). Objective determination of cloud heights and radar reflectivities using a combination of active remote sensors at the ARM CART sites. *Journal of Applied Meteorology*, *39*(5), 645–665. https://doi.org/10.1175/1520-0450(2000)039%3C0645:ODOCHA%3E2.0.CO;2

Dai, A. (2006). Precipitation characteristics in eighteen coupled climate models. *Journal of Climate*, *19*(18), 4605–4630. https://doi.org/10.1175/JCLI3884.1

Del Genio, A. D., & Wu, J. (2010). The role of entrainment in the diurnal cycle of continental convection. *Journal of Climate*, *23*(10), 2722–2738. https://doi.org/10.1175/2009JCLI3340.1

Field, P. R., & Wood, R. (2007). Precipitation and cloud structure in midlatitude cyclones. *Journal of Climate*, *20*(2), 233–254. https://doi.org/10.1175/JCLI3998.1

Giangrande, S. E., Collis, S., Theisen, A., & Tokay, A. (2014). Precipitation estimation from the ARM distributed radar network during the MC3E campaign. *Journal of Applied Meteorology and Climatology*, *53*(9), 2130–2147. https://doi.org/10.1175/JAMC-D-13-0321.1

Giangrande, S. E., Luke, E. P., & Kollias, P. (2012). Characterization of vertical velocity and drop size distribution parameters in widespread precipitation at ARM facilities. *Journal of Applied Meteorology and Climatology*, *51*(2), 380–391. https://doi.org/10.1175/JAMC-D-10-05000.1

Grabowski, W. W., Bechtold, P., Cheng, A., Forbes, R., Halliwell, C., Khairoutdinov, M., et al. (2006). Daytime convective development over land: A model intercomparison based on LBA observations. *Quarterly Journal of the Royal Meteorological Society*, *132*(615), 317–344. https://doi.org/10.1256/qj.04.147

Gustafson, W. I., Vogelmann, A. M., Cheng, X., Endo, S., Krishna, B., Li, Z., et al. (2017). In R. Stafford (Ed.), *Recommendations for implementation of the LASSO Workflow*, *DOE/SC-ARM-17-031* (p. 62). DOE Atmospheric Radiation Measurement Climate Research Facility. https://doi.org/10.2172/1406259

Jensen, M. P., Petersen, W. A., Bansemer, A., Bharadwaj, N., Carey, L. D., Cecil, D. J., et al. (2016). The Midlatitude Continental Convective Clouds Experiment (MC3E). *Bulletin of the American Meteorological Society*, *97*(9), 1667–1686. https://doi.org/10.1175/BAMS-D-14-00228.1

Jensen, M. P., Toto, T., Troyan, D., Ciesielski, P., Holdridge, D., Kyrouac, J., et al. (2015). The MC3E sounding network: Operations, processing and analysis. *Atmospheric Measurement Techniques*, *8*(1), 1–18. https://doi.org/10.5194/amt-8-1-2015

Khairoutdinov, M., & Kogan, Y. (2000). A new cloud physics parameterization in a large-eddy simulation model of marine stratocumulus. *Monthly Weather Review*, *128*(1), 229–243. https://doi.org/10.1175/1520-0493(2000)128%3C0229:ANCPPI%3E2.0.CO;2

Khairoutdinov, M. F., & Randall, D. A. (2003). Cloud resolving modeling of the ARM summer 1997 IOP: Model formulation, results, uncertainties, and sensitivities. *Journal of the Atmospheric Sciences*, *60*(4), 607–625. https://doi.org/10.1175/1520-0469(2003)060%3C0607:CRMOTA%3E2.0.CO;2

Kim, K.-M., Lau, W. K. M., Sud, Y. C., & Walker, G. K. (2010). Influence of aerosol–radiative forcings on the diurnal and seasonal cycles of rainfall over West Africa and eastern Atlantic Ocean using GCM simulations. *Climate Dynamics*, *35*(1), 115–126. https://doi.org/10.1007/s00382-010-0750-1

Kollias, P., & Albrecht, B. (2000). The turbulence structure in a continental stratocumulus cloud from millimeter-wavelength radar observations. *Journal of the Atmospheric Sciences*, *57*(15), 2417–2434. https://doi.org/10.1175/1520-0469(2000)057%3C2417:TTSIAC%3E2.0.CO;2

Kollias, P., Albrecht, B. A., Clothiaux, E. E., Miller, M. A., Johnson, K. L., & Moran, K. P. (2005). The atmospheric radiation measurement program cloud profiling radars: An evaluation of signal processing and sampling strategies. *Journal of Atmospheric and Oceanic Technology*, *22*(7), 930–948. https://doi.org/10.1175/JTECH1749.1

Kollias, P., Jo, I., Borque, P., Tatarevic, A., Lamer, K., Bharadwaj, N., et al. (2014). Scanning ARM cloud radars. Part II: Data quality control and processing. *Journal of Atmospheric and Oceanic Technology*, *31*(3), 583–598. https://doi.org/10.1175/JTECH-D-13-00045.1

Matheou, G., Chung, D., Nuijens, L., Stevens, B., & Teixeira, J. (2011). On the fidelity of large-eddy simulation of shallow precipitating cumulus convection. *Monthly Weather Review*, *139*(9), 2918–2939. https://doi.org/10.1175/2011MWR3599.1

Mather, J. H., & Voyles, J. W. (2013). The ARM climate research facility: A review of structure and capabilities. *Bulletin of the American Meteorological Society*, *94*(3), 377–392. https://doi.org/10.1175/BAMS-D-11-00218.1

Mechem, D. B., Giangrande, S. E., Fish, C. S., Borque, P., Toto, T., & Kollias, P. (2015). Insights from modeling and observational evaluation of a precipitating continental cumulus event observed during the MC3E field campaign. *Journal of Geophysical Research: Atmospheres*, *120*, 1980–1995. https://doi.org/10.1002/2014JD022255

Mechem, D. B., Kogan, Y. L., & Schultz, D. M. (2010). Large-eddy simulation of post-cold-frontal continental stratocumulus. *Journal of the Atmospheric Sciences*, *67*(12), 3835–3853. https://doi.org/10.1175/2010JAS3467.1

Mechem, D. B., & Oberthaler, A. J. (2013). Numerical simulation of tropical cumulus congestus during TOGA COARE. *Journal of Advances in Modeling Earth Systems*, *5*, 1–15. https://doi.org/10.1002/jame.20043

Medeiros, B., & Stevens, B. (2011). Revealing differences in GCM representations of low clouds. *Climate Dynamics*, *36*(1-2), 385–399. https://doi.org/10.1007/s00382-009-0694-5

Medeiros, B., Stevens, B., Held, I. M., Zhao, M., Williamson, D. L., Olson, J. G., & Bretherton, C. S. (2008). Aquaplanets, climate sensitivity, and low clouds. *Journal of Climate*, *21*(19), 4974–4991. https://doi.org/10.1175/2008JCLI1995.1

Mesinger, F., Di Mego, G., Kalnay, E., Mitchell, K., Shafran, P. C., Ebisuzaki, W., et al. (2006). North American regional reanalysis. *Bulletin of the American Meteorological Society*, *87*(3), 343–360. https://doi.org/10.1175/BAMS-87-3-343

Morrison, H., Curry, J. A., & Khvorostyanov, V. I. (2005). A new double-moment microphysics parameterization for application in cloud and climate models. Part I: Description. *Journal of the Atmospheric Sciences*, *62*(6), 1665–1677. https://doi.org/10.1175/JAS3446.1

Oue, M., Kollias, P., North, K. W., Tatarevic, A., Endo, S., Vogelmann, A. M., & Gustafson, W. I. Jr. (2016). Estimation of cloud fraction profile in shallow convection using a scanning cloud radar. *Geophysical Research Letters*, *43*, 10,998–11,006. https://doi.org/10.1002/2016GL070776

Rauber, R. M., Stevens, B., Ochs, H. T. III, Knight, C., Albrecht, B. A., Blyth, A. M., et al. (2007). Rain in Shallow Cumulus Over the Ocean: The RICO Campaign. *Bulletin of the American Meteorological Society*, *88*, 1912–1928. https://doi.org/10.1175/BAMS-88-12-1912

Siebesma, A. P., Bretherton, C. S., Brown, A., Chlond, A., Cuxart, J., Duynkerke, P. G., et al. (2003). A large-eddy simulation study of shallow cumulus convection. *Journal of the Atmospheric Sciences*, *60*(10), 1201–1219. https://doi.org/10.1175/1520-0469(2003)60%3C1201:ALESIS%3E2.0.CO;2

Song, H., Lin, W., Lin, Y., Wolf, A., Neggers, R., Donner, L. J., et al. (2013). Evaluation of precipitation simulated by seven SCMs against the ARM observation at the SGP site. *Journal of Climate*, *26*(15), 5467–5492. https://doi.org/10.1175/JCLI-D-12-00263.1

Stevens, B., Ackerman, A. S., Albrecht, B. A., Brown, A. R., Chlond, A., Cuxart, J., et al. (2001). Simulations of trade wind cumuli under a strong inversion. *Journal of the Atmospheric Sciences*, *58*(14), 1870–1891. https://doi.org/10.1175/1520-0469(2001)058%3C1870:SOTWCU%3E2.0.CO;2

Stevens, B., & Bony, S. (2013). What are climate models missing? *Science*, *340*(6136), 1053–1054. https://doi.org/10.1126/science.1237554

Stevens, B., Moeng, C. H., Ackerman, A. S., Bretherton, C. S., Chlond, A., de Roode, S., et al. (2005). Evaluation of large-eddy simulations via observations of nocturnal marine stratocumulus. *Monthly Weather Review*, *133*(6), 1443–1462. https://doi.org/10.1175/MWR2930.1

Van Zanten, M. C., Stevens, B., Nuijens, L., Siebesma, A. P., Ackerman, S., Burnet, F., et al. (2011). Controls on precipitation and cloudiness in simulations of trade-wind cumulus as observed during RICO. *Journal of Advances in Modeling Earth Systems*, *3*, M06001. https://doi.org/10.3894/JAMES.2011.3.5

Wu, C.-M., Lo, M.-H., Chen, W.-T., & Lu, C.-T. (2015). The impacts of heterogeneous land surface fluxes on the diurnal cycle precipitation: A framework for improving the GCM representation of land-atmosphere interactions. *Journal of Geophysical Research: Atmospheres*, *120*, 3714–3727. https://doi.org/10.1002/2014JD023030

Wu, C. M., Stevens, B., & Arakawa, A. (2009). What controls the transition from shallow to deep convection? *Journal of the Atmospheric Sciences*, *66*(6), 1793–1806. https://doi.org/10.1175/2008JAS2945.1

Wyant, M. C., Bretherton, C. S., Chlond, A., Griffin, B. M., Kitagawa, H., Lappen, C. L., et al. (2007). A single-column model intercomparison of a heavily drizzling stratocumulus-topped boundary layer. *Journal of Geophysical Research*, *112*, D24204. https://doi.org/10.1029/2007JD008536

Xie, S., Zhang, M. H., Branson, M., Cederwall, R. T., Del Genio, A. D., Eitzen, Z. A., et al. (2005). Simulations of midlatitude frontal clouds by single-column and cloud-resolving models during the Atmospheric Radiation Measurement March 2000 cloud intensive operational period. *Journal of Geophysical Research*, *110*, D15S03. https://doi.org/10.1029/2004JD005119

Xie, S., Zhang, Y., Giangrande, S. E., Jensen, M. P., McCoy, R., & Zhang, M. (2014). Interactions between cumulus convection and its environment as revealed by the MC3E sounding array. *Journal of Geophysical Research: Atmospheres*, *119*, 11,784–11,808. https://doi.org/10.1002/2014JD022011

Xu, K.-M., Cederwall, R. T., Donner, L. J., Grabowski, W. W., Guichard, F., Johnson, D. E., et al. (2002). An intercomparison of cloud-resolving models with the Atmospheric Radiation Measurement summer 1997 Intensive Observation Period data. *Quarterly Journal of the Royal Meteorological Society*, *128*(580), 593–624. https://doi.org/10.1256/003590002321042117

Xu, K.-M., Zhang, M. H., Eitzen, M. A., Ghan, S. J., Klein, S. A., Wu, X. Q., et al. (2005). Modeling springtime shallow frontal clouds with cloud-resolving and single-column models. *Journal of Geophysical Research*, *110*, D15S04. https://doi.org/10.1029/2004JD005153

Yuan, W., Yu, R., Zhang, M., Lin, W., Li, J., & Fu, Y. (2013). Diurnal cycle of summer precipitation over subtropical East Asia in CAM5. *Journal of Climate*, *26*(10), 3159–3172. https://doi.org/10.1175/JCLI-D-12-00119.1

Zhang, J., Howard, K., & Gourley, J. J. (2005). Constructing three-dimensional multiple-radar reflectivity mosaics: Examples of convective storms and stratiform rain echoes. *Journal of Atmospheric and Oceanic Technology*, *22*(1), 30–42. https://doi.org/10.1175/JTECH-1689.1

Zhang, Y., & Klein, S. A. (2013). Factors controlling the vertical extent of fair-weather shallow cumulus clouds over land: Investigation of diurnal-cycle observations collected at the ARM Southern Great Plains site. *Journal of the Atmospheric Sciences*, *70*(4), 1297–1315. https://doi.org/10.1175/JAS-D-12-0131.1

Zhang, M. H., & Lin, J. L. (1997). Constrained variational analysis of sounding data bases on column-integrated budgets of mass, heat, moisture, and momentum: Approach and application to ARM measurements. *Journal of the Atmospheric Sciences*, *54*(11), 1503–1524. https://doi.org/10.1175/1520-0469(1997)054%3C1503:CVAOSD%3E2.0.CO;2

Zuidema, P., Torri, G., Muller, C., & Chandra, A. (2017). A survey of precipitation-induced atmospheric cold pools over oceans and their interactions with the larger-scale environment. *Surveys in Geophysics*, *38*(6), 1283–1305. https://doi.org/10.1007/s10712-017-9447-x